Quantifying silo flow using MRI velocimetry for testing granular flow models

Luke Fullard*
School of Fundamental Sciences, and Massey University, New Zealand

Daniel J. Holland
Department of Chemical and Process Engineering, University of Canterbury, New Zealand

Petrik Galvosas
School of Chemical and Physical Sciences, Victoria University, New Zealand

Clive Davies
School of Food and Advanced Technology, Massey University, New Zealand

Pierre-Yves Lagrée and Stéphane Popinet
Institut Jean le Rond d'Alembert, CNRS UMR 7190 Sorbonne Université, Paris, France

(Received 6 March 2019; published 3 July 2019)

In this work we present experimental results of the gravity-driven discharge of poppy seeds from three-dimensionally (3D) printed silos. The velocity fields of the flowing poppy seeds are measured using magnetic resonance imaging (MRI) velocimetry techniques. Crucially, this approach allows the velocity field to be determined throughout the flow domain, unlike visual techniques such as particle image velocimetry and related methods where only the flow at or near the wall is accessible. We perform the experiment three times; with 3D-printed silos of cone half angles 30° and 50°, respectively, and then repeat the 30° silo experiment but with a layer of poppy seeds glued to the silo wall to create a "rough wall" condition. In our experiments, we observe and quantify velocity fields for three well-known granular flow regimes; mass flow, funnel flow, and rat-holing. The results of the experiments are compared to equivalent output of numerical simulations. In this mathematical model, the well-known $\mu(I)$ friction law is used to define an effective granular viscosity, and the flow is solved using a standard Navier-Stokes type solver. While the results are generally encouraging, it is noted that some aspects of the model are lacking and should be improved; in particular, the rat-holing effect observed in one of the MRI experiments was not predicted by the model, nor was the exact volumetric flow rate from any of the silos. Suggestions for model improvement are discussed.

DOI: 10.1103/PhysRevFluids.4.074302

I. BACKGROUND AND INTRODUCTION

Granular matter is well known to behave in complex and often unexpected ways. Particles in a granular assembly may act in a solidlike, liquidlike, or gaslike manner, with the transition between these phases often difficult to define and quantify [1]. A commonly studied granular system is gravity-driven silo In addition to being a system of great practical importance, silo flow can also display a variety of interesting flow dynamics. Depending on the design of the silo (i.e., the silo

*l.fullard@massey.ac.nz

half angle, the friction between particles, the friction between the silo walls and particles, and the size and shape of the particles), the flow may be either mass flow or funnel flow or display rat-holing [2,3]. In mass flow, all particles in the silo are in motion with no stagnant zones; in funnel flow there are regions within the silo where particles flow, but there are also stagnant regions (and an interface between flowing/stagnant regions); when a silo displays rat-holing, flow only occurs in a central core approximately the size of the silo opening, with large stagnant regions surrounding this core. Rat-holing can be considered an extreme case of funnel flow, but the flow is often observed to be intermittent and transient, whereas in a general funnel flow the dynamics are much more steady. Due to the variety of flow regimes, the silo provides an excellent test of numerical models of granular dynamics.

Apart from testing numerical codes, quantifying velocity fields in the silo is of great industrial importance, for example, in the study of particle mixing and segregation as particle blends are discharged from a silo. While there have been many discrete element modelling (DEM) [4–6] and continuum models [7–14] developed to study the silo, experimental measurements and validations are still required.

The vast majority of experimental characterization of the velocity vector field in a discharging silo has been using visual imaging methods in transparent silos (both conical and planar). Techniques such as particle image velocimetry (PIV) and particle tracking velocimetry (PTV) have been successfully applied to measure the grain velocity *at the silo walls* [15–20]. On the contrary, however, experimental measurements of velocity fields away from silo walls (i.e., in the bulk of the flow) are particularly difficult to obtain. Previous attempts to experimentally quantify 3D velocity fields in silos have included x-ray computed tomography (CT) [21,22], timing tracer discharge [23], scanning γ-ray tomography [24,25], and single profile proton absorptiometry [26]; however, all of these methods give limited velocity profile information and usually provide averaged data, data at discrete points, or data along a line only rather than on a plane.

Magnetic resonance imaging (MRI) is an alternative technique that can study flow in optically opaque systems. MRI has been applied to nonsilo granular systems [27–34] to quantify parameters such as velocity fields and packing. Kawaguchi [35] observed the flow type, either mass or funnel flow, in silos using tagged MR imaging. In this approach, bands of particles are tagged at one point in time and then the positions of these tagged particles imaged after a defined delay (in this case 100 ms). The deformation of the tagged layers was observed visually. In theory this technique could be extended to estimate the velocity in a silo using further image processing techniques, but this would give only an indirect measure of the velocity fields. MRI has also been used to obtain the only reported direct, quantitative measurement of the silo velocity data on a plane away from the silo walls that we have found [36], though the range of silo flow conditions studied was limited. The first objective of the current article is to extend the work of Gentzler and Tardos [36] to obtain velocity field data for a wider range of silo flow situations. First, we report on both the vertical and horizontal component of the velocity at the outlet. Second, we also measure particles of a large diameter ($\approx$1 mm) such that the effect of the surrounding air on the particle dynamics near the orifice is not significant [37]. Third, we consider the effect of changing the hopper geometry. Finally, we consider the effect of rough walls on the particle dynamics. These last two aspects of the experiment mean that flow is studied across the three major flow regimes observed in silos.

A second objective is to assess the applicability of the so-called $\mu(I)$ friction law [38] for reproducing the velocity fields which we experimentally measure. Previously, the $\mu(I)$ friction law has been used to define an effective granular viscosity for use in incompressible continuum flow models. Such an approach has been successfully applied to the granular column collapse and to some silo flows [7,8,13,39]. However, the velocity fields produced by the model have not been rigorously tested against experimental data. In particular, we examine the model applicability to reproduce the three silo flow modes, mass flow, funnel flow, and rat-holing, which we observe in our experimental results.

II. MATERIALS AND METHODS

A. Particle properties

In this study, poppy seeds were chosen as the granular material of interest due to their particle size, their price and availability, and the fact that they contain abundant free oil which allows a strong signal to be detected by the MRI equipment. The poppy seeds were nonspherical and were kidney shaped, as seen in Fig. 1. The poppy long diameter was approximately 1.25 mm, while the short diameter was approximately 0.85 mm. A standard sieve experiment was performed and ≈93% of the particles were found to be between 710 and 1180 μm, with a Sauter mean diameter [40], d, of 951 μm.

B. Silo system design

The silo feeding system was designed to the specifications of the bore of the MRI apparatus in such a way that the poppy seeds were fully contained and never came in direct contact with the MRI apparatus itself. A system of perspex pipes of decreasing diameter was used to feed the poppy seeds into the test silo (the region to be imaged by the MRI) and then out of the bottom of the system. These pipes were connected using a series of push-fittings with small tolerances. Figure 2(a) displays the full system of pipes and the test silo, while Fig. 2(b) is a close up of the silo itself. The silo was designed in a CAD program and 3D printed from ABS plastic, and the opening at the bottom of the silo, D_0, was drilled to a diameter of 6.5 mm (note that this is ≈6.5 times greater than the Sauter mean diameter, d, of the particles to avoid jamming [18,41]). The inner diameter of the silo, W, was 23.5 mm. Since $D_0 > 6.5d$, $W > 2.5D_0$, and the bed height is always deeper than the silo opening diameter, the flow rate from the silo can be expected to be independent of the silo geometry [42]. The silo half angle, ϕ, was changed between each experiment; the first silo had a 30° half angle, the second 50°, and the third was another 30° half-angled silo but with rough walls. The rough walled silo was printed in two halves, and then poppy seeds were glued onto the inner silo walls in a single layer, and, finally, the two halves were glued together to form a full silo. We note that the diameter of the final pipe, labeled pipe 3 in Fig. 2, was wider than the silo opening. This design was to avoid the well-known standpipe flow rate effect [43] which does not occur unless the pipe below the silo is full [43]. Since the silo opening diameter was smaller than the exit pipe this was not the case and the standpipe effect was avoided.

C. Experimental method

A Bruker Avance I Nuclear Magnetic Resonance spectrometer with a 9.4-T wide bore magnet located at Victoria University of Wellington, New Zealand, was used for the experiments. A 30-mm-diameter radio-frequency coil was used for excitation and detection. A three-axis shielded Micro2.5 gradient set capable of producing a maximum gradient strength of 1.51 T m^{-1} was used for imaging and flow encoding. The pipes and silo were connected together and carefully inserted into the MRI. The silo and upper two pipes were filled from above through a funnel. A bucket was placed under the system to collect the discharged particles. As the particles were discharged the system was periodically refilled from above such that the upper pipe (pipe 1) was never more than half empty. Note that the flow rate from the silo was constant and independent of fill height as is implicit in the Beverloo flow rate equation [44,45].

The vertical (i.e., in the axial direction) and horizontal (i.e., in the radial direction) components of velocity of the poppy seeds were measured using a phase-encoded velocity imaging sequence [46]. The image was obtained using a spin echo acquisition with a slice selective refocusing pulse. To enable accurate measurements of the wide range of velocities present in the system, experiments were repeated with eight flow encoding gradients. The velocity was calculated from a linear fit to as many of these data points as possible. For the fastest flowing regions, typically only three experiments with the weakest flow encoding gradients were used, while in the slow-moving regions all eight experiments were used. The gradient encoding duration δ was set to 0.7 ms, the observation

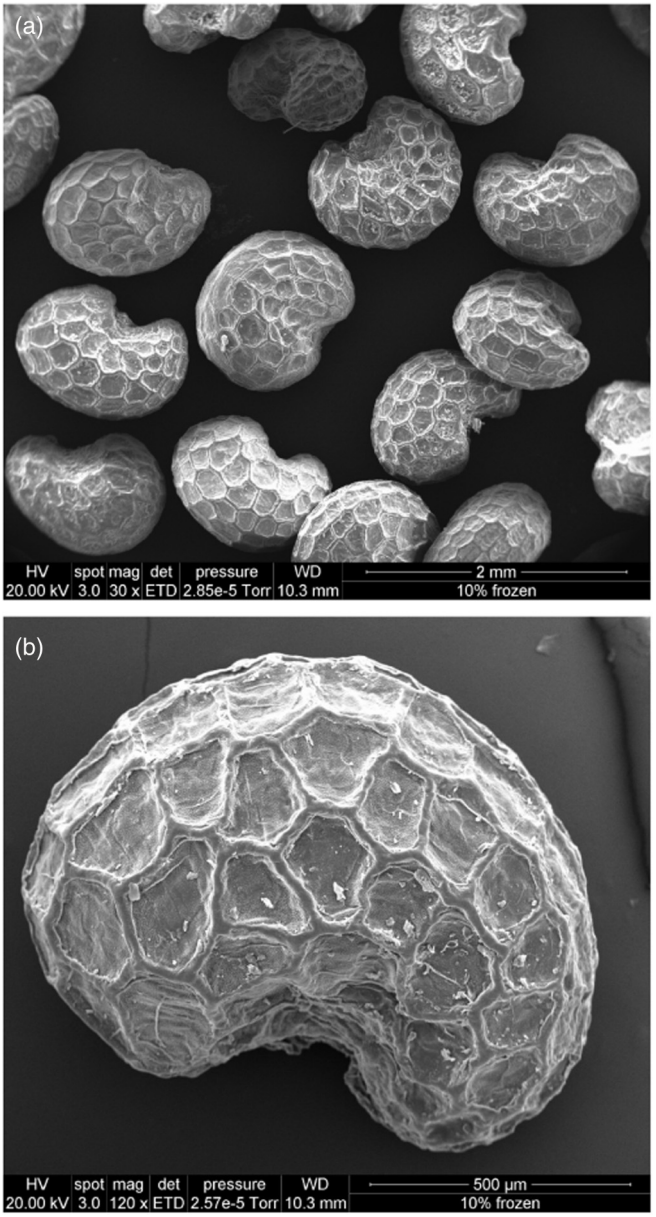

FIG. 1. Scanning electron microscope images of a sample of poppy seeds. It is apparent from the image that the seeds are nonspherical with a kidney shape. The surface of the seeds is also seen to be textured. A scale is included at the bottom of each image. (a) An image of multiple poppy seeds. (b) A close up of a single poppy seed.

time was 2.5 ms, and the maximum gradient strength was set to 0.07 T m^{-1} in the vertical direction and 0.14 T m^{-1} in the horizontal direction. These settings gave a maximum field of flow of approximately 2 m s^{-1} with a minimum detectable velocity of 1×10^{-3} m s^{-1}, where the minimum detectable velocity corresponds to a signal-to-noise ratio for the phase of 2. Images were acquired at a spatial resolution of 0.45 mm in the horizontal direction and 1.18 mm in the vertical direction

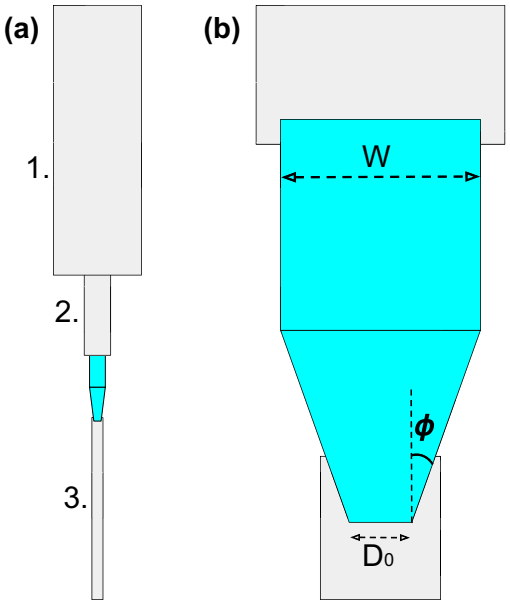

FIG. 2. A sketch of the piping and silo in the experimental set-up (not to scale). (a) The system is loaded from above. The seeds flow through the largest pipe 1 into the more narrow pipe 2 through the test silo section and out through pipe #3. (b) A close up of the test silo section.

with a slice thickness of 1 mm. The total acquisition time for the images was approximately 50 min. Flow-encoded NMR images can acquire a phase arising from the imaging gradients themselves. It is common practice to correct this phase by acquiring measurements on a static sample. Here images of a static bed were also acquired. The phase change for these was negligible, and thus no correction was required.

Three MRI experiments were performed, one with a silo of 30° half angle, one with a silo of 50° half angle, and, finally, with another silo of 30° half angle but with rough walls (with particles glued on the silo walls).

D. Numerical model

One goal of this work is to model the silo using a continuum model of granular flow. Recently, the $\mu(I)$ law for the friction of granular materials has been used to define an effective viscosity in granular flow simulations. This viscosity was successfully implemented into an incompressible Navier-Stokes solver (Gerris Flow Solver [47]) to model dense granular flow in a variety of situations [7,8,13,39]. For our situation, an axisymmetric domain was used so that our 3D silo could be modelled in 2D. The governing equations of incompressible flow were solved in Gerris,

$$\nabla \cdot \mathbf{u} = 0, \tag{1}$$

$$\rho\left(\frac{\partial \mathbf{u}}{\partial t} + \mathbf{u} \cdot \nabla \mathbf{u}\right) = -\nabla p + \nabla \cdot (2\eta \mathbf{D}) + \rho \mathbf{g}. \tag{2}$$

In the above continuity and momentum equations, $\mathbf{u}$ is the velocity vector, ρ the flowing (bulk) density, p the local isotropic pressure, η the effective (or apparent) granular viscosity, and $\mathbf{D}$ the rate of strain tensor. The effective viscosity is defined as

$$\eta_{\text{eff}} = \frac{\mu(I)p}{D_2}, \tag{3}$$

TABLE I. Parameters used in the numerical model.

Name	Symbol	Unit	Value
Bulk density	ρ	kg/m^3	600
Particle density	ρ_p	kg/m^3	1000
Particle diameter	d	mm	0.951
Friction coefficient 1	μ_1	–	0.6
Friction coefficient 2	μ_2	–	1.7
Reference inertial number	I_0	–	0.5

but in practice a regularized effective viscosity was used to avoid infinite values when the fluid is experiencing small shear,

$$\eta = \min\left[\frac{\mu(I)p}{D_2}, \eta_{\max}\right]. \tag{4}$$

Here $D_2 = \sqrt{\frac{1}{2}D_{ij}D_{ij}}$ is the second invariant of the strain rate tensor, where $D_{ij} = \frac{\partial u_i}{\partial x_j} + \frac{\partial u_j}{\partial x_i}$, and $\mu(I)$ is the granular friction law,

$$\mu(I) = \mu_1 + \frac{\mu_2 - \mu_1}{I_0/I + 1}, \tag{5}$$

with μ_1, μ_2, and I_0 parameters. The variable I is the granular inertial number and is defined as

$$I = \frac{dD_2\sqrt{\rho_p}}{\sqrt{p}}, \tag{6}$$

where d is the particle diameter and ρ_p is the solid particle density.

In our axisymmetric numerical model we apply no-slip conditions on both of the velocity components at the silo walls, a symmetry condition along the axis of symmetry, and homogeneous Neumann velocity boundary conditions (for each velocity component) at the top and bottom of the silo, and we set $p = 0$ at the top and bottom of the silo. Note that other boundary conditions could be used at the silo wall (for example, to allow slip at the silo wall [48,49]), but the effect of more complex boundary conditions is left for future work. For the 30° silo with rough walls, the simulation domain was reduced by a particle diameter in size to account for the reduced dimensions due to the layer of particles glued to the silo walls, but the silo opening was kept at 6.5 mm. No other change to the boundary conditions was made.

Parameters used in our simulation are listed in Table I. The first friction parameter, μ_1, was chosen based on measurements of the angle of repose of the poppy seeds which was found to be approximately 31°, and, hence, $\mu_1 = \tan 31 = 0.6$. The upper limit on the friction angle, defined by parameter $\tan^{-1}(\mu_2)$, was expected to be around 60° since our MRI experimental results for the velocity in the 30° silo (to be presented in Fig. 3) showed small slow/stagnant regions at the transition from the conical to cylindrical section. We also noted that larger values of I_0 kept the incompressible $\mu(I)$ model in the well-posed regime for a wider range of inertial numbers than for low values of I_0 [50]. For this reason, various values of $\tan^{-1}(\mu_2) \approx 60°$ and I_0 between 0.05 and 1 were tested. It was found that the parameters $\mu_2 = 1.7$ and $I_0 = 0.5$ gave a good match to experimental data (to be discussed), gave a wide range of well-posed inertial number values, and, importantly, were physically realistic.

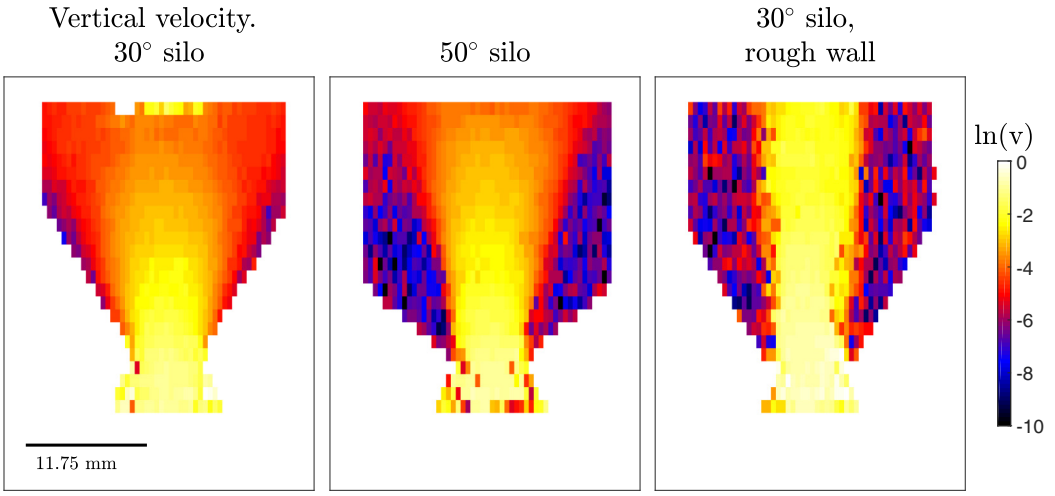

FIG. 3. The log of the magnitude of the vertical component of velocity (v) is plotted for each of the three silos. Mass flow is observed in the 30° silo, funnel flow in the 50°, and rat-holing in the 30° silo with rough walls (with particles glued to the silo wall). Yellow regions indicate rapid flow, while purple/blue areas indicate slow to stagnant zones.

III. RESULTS

A. MRI experimental results

The results of the phase-encoded velocity imaging sequence experiment were converted into a Matlab data file and plotted as a contour map. In Fig. 3 the logarithm of the vertical component of velocity is plotted for each of the three silos, where $\mathbf{u} = (u, v)$ is the velocity vector with u and v the horizontal and vertical velocity components, respectively. The logarithm of the magnitude of the horizontal component of velocity (u) is shown in Fig. 4. The lighter (yellow) regions are zones of rapid flow, while the darker (purple/blue) regions indicate slow or stagnant flow. Horizontal velocity measurements were not available for the 30° silo with rough walls because the magnitude of the

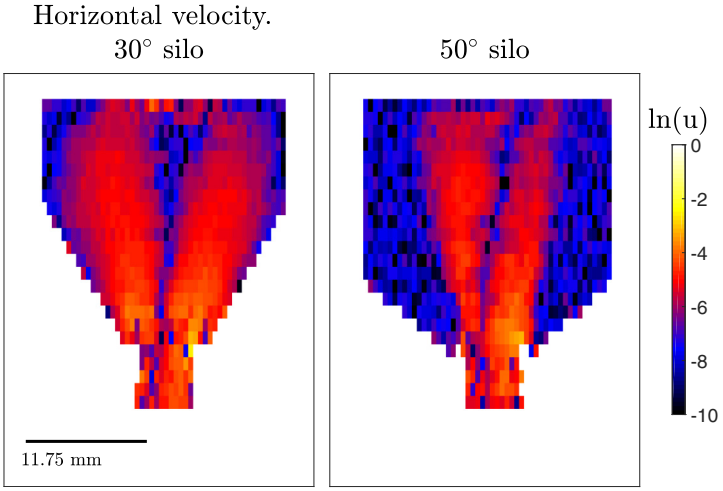

FIG. 4. The log of the magnitude of the horizontal component of velocity (u) for the 30° and 50° silos.

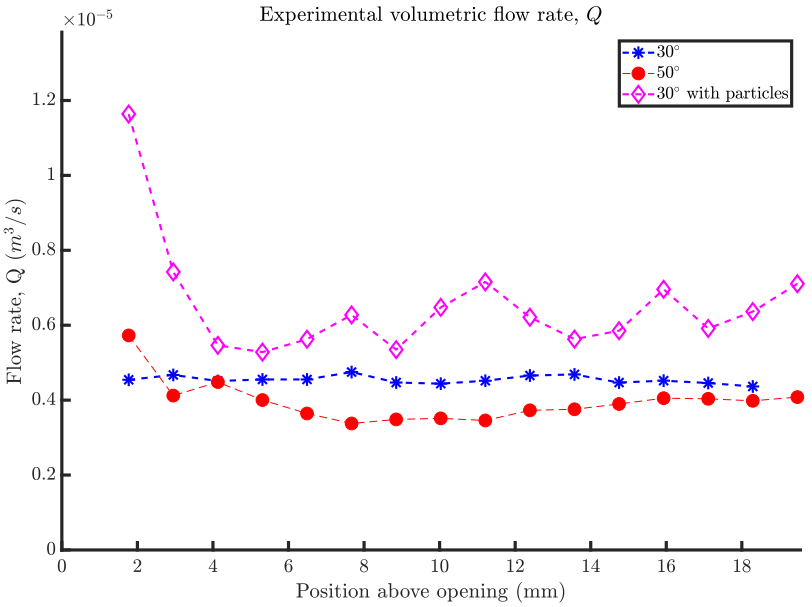

FIG. 5. The volumetric flow rate, $Q(z)$, for each of the three silo experiments as a function of height above the silo opening.

horizontal component of velocity was very small and was of the same order as the noise in the experiment.

The most immediate observation from Fig. 3 is that for each silo we have a different flow regime. In the 30° silo we observe mass flow. The particles in the silo at every location are in motion, with a possible small exception at the transition from the cone to the cylindrical section. In the 50° silo we observe funnel flow. There is a region of flow in the center of the silo and this region of flowing material widens as we move further up into the silo. There is a clear stagnant region of flow that surrounds the flowing particles. This stagnant region shrinks as we transition higher into the silo. In the 30° silo with rough walls (i.e., with a layer of poppy seeds glued to the wall) we observe the rat-holing effect. There is a fast core (roughly the diameter of the silo opening) of flowing particles surrounded by a region of stagnant material. The size of this stagnant zone does not perceptibly change as we transition higher into the silo. It is also apparent that the velocity field in the flowing zone remains continuous as we move higher in the silo, past the transition from the conical to cylindrical section (i.e., we do not observe velocity discontinuities or shocks). This is in contrast to predictions from Mohr-Coulomb plasticity-based models [2,51].

In order to assess the appropriateness of the incompressible assumption in our numerical model, we quantify the volumetric flow rate as a function of height above the silo opening. For each MRI experiment we use the vertical component of velocity (v) to calculate the volumetric flow rate,

$$Q(z) = 2\pi \int_{r(z)=0}^{r(z)=R(z)} vrdr, \tag{7}$$

where $r(z)$ is the radial coordinate from the axis of the silo and $R(z)$ is the radius of the silo at height z above the opening. The resulting flow rates for each experiment are plotted in Fig. 5.

It is apparent from the figure that the volumetric flow rate is approximately constant throughout the silo in the 30° silo, but this is not so for the 50° and 30° silo with roughened walls. In these two nonconstant flow rate cases, the volumetric flow rate $Q(z)$ is seen to be $\approx 2\times$ higher near the opening than it is in the bulk of the silo. This variation in flow rate could arise either from a measurement

error or a dilation of the flow at the outlet. The signal intensity at the outlet in all three images is less than half that in the bulk, which would be consistent with a dilation of the flow at the outlet. However, in these measurements there is also significant attenuation of the signal due to the motion of the particles, so the images are not quantitative in solid fraction. Therefore it is important to consider the errors that arise in measurement of velocity. MRI measurements of the velocity are prone to error in regions of high velocity, but this error will tend to cause an underestimation of the velocity as faster-moving particles are more heavily attenuated than slower-moving particles. The flow rate is seen to increase toward the outlet and, hence, it is unlikely that a velocity measurement error could explain the observed flow rate variation. Therefore, it is concluded that, for the funnel-flow and rat-holing silos, there is significant dilation of the flow near the opening, and the assumption of incompressibility is likely to be erroneous, at least near the silo opening. In a similar system, a wedge-shaped hopper, a significant reduction in bulk density has been observed [52]. As a point of context, in the numerical model the incompressibility condition is enforced (up to a tolerance) and it was found that the change in the volumetric flow rate was less than 1% throughout the silo. Here we assume that the use of an incompressible flow model has only a small effect on the predicted velocity fields, since in the bulk of the silo the flow rate is relatively constant, changing only near the silo opening. However, the dilation near the opening will change the predicted flow rate values. Given this result and model assumption, when comparing experimental and numerical results with an incompressible flow assumption, the velocity should be adjusted to account for the change in volumetric flow rate. In practice this is achieved by normalizing the velocity by the volumetric flow rate at each local height above the silo opening. Furthermore, we quantified the mass flow rate, $\dot{m}$, from each of the silos by measuring the mass ejected from the system in a given time. For the 30° silo we found $\dot{m}_{30} = 2.11 \pm 0.07$ g/s, for the 50° silo $\dot{m}_{50} = 1.74 \pm 0.09$ g/s, and for the 30° silo with particles on the wall $\dot{m}^{p}_{30} = 2.2 \pm 0.1$ g/s. The reduction of the mass flow rate between the 30° and 50° silos is compared with corrections made to the Beverloo flow rate to account for hopper half angle [53]. Assuming that the Beverloo parameters and bulk density is equal between the two silos of differing half angles, the ratio of the two flow rates is given as $M = \frac{f(50^\circ)}{f(30^\circ)}$, where the function $f(\alpha) = \sqrt{\frac{1-\cos\alpha}{2\sin^3\alpha}}$. The theoretical ratio M is calculated as 0.86, while the experimental ratio in our system, $\frac{\dot{m}_{50}}{\dot{m}_{30}}$, is found to be 0.82 ± 0.05, in good agreement with the theoretical value.

B. Numerical model results: 30° silo

To directly compare the $\mu(I)$ numerical results to the MRI experimental results, a results file was imported from Gerris into Matlab which contained vertical and horizontal components of velocity. These data were interpolated onto five horizontal lines which correspond to the locations of measurements taken in the MRI experiments. Thus, the horizontal and vertical components of velocity predicted in the model could be directly compared to the experimental data.

As previously mentioned, the volumetric flow rate in the silo experiments was not a constant near the opening of the silo. Therefore, both the experimentally measured and numerically predicted velocity data were normalized by the volumetric flow rate before being compared. At each height above the silo opening, z, the local volumetric flow rate is calculated using Eq. (7). The velocity components are then multiplied by the particle diameter squared and divided by the local volumetric flow rate to obtain the normalized velocity, $\tilde{\mathbf{u}}$, where $\tilde{\mathbf{u}} = \mathbf{u}d^2/Q$.

The comparison of the vertical velocity profile taken at five heights above the opening for the 30° silo with smooth walls (i.e., no particles attached to the wall) is shown in Fig. 6, while the horizontal velocity profile is shown in Fig. 7. The distance from the silo opening to the silo transition (the point where the cone becomes a cylinder) is ≈14.7 mm, and hence four of the comparison lines are in the converging conical section of the silo, while one is in the cylindrical section.

It is apparent that the match between the experimentally derived and numerically predicted normalized velocity is good, particularly for the vertical velocity. The normalized velocity predicted by the model has approximately the same maximum and also approximately the same curvature and

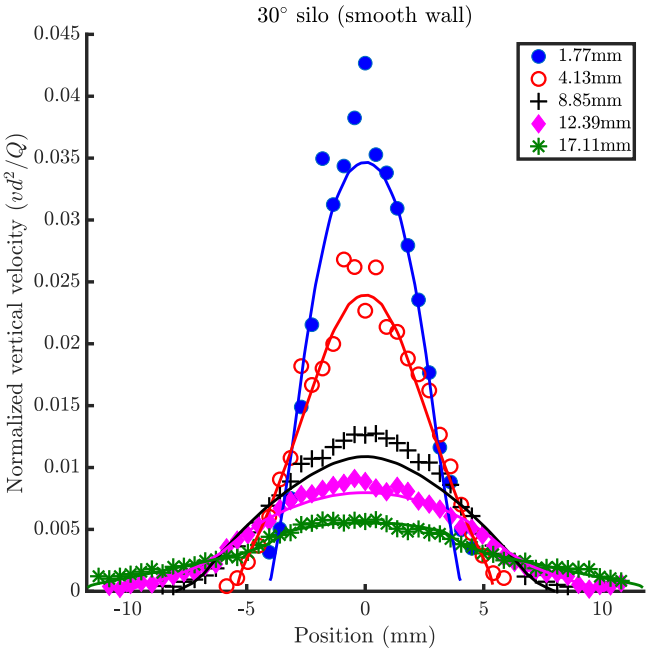

FIG. 6. The vertical velocity MRI measurements (solid circles) compared with those predicted by the numerical model (lines) for the 30° silo.

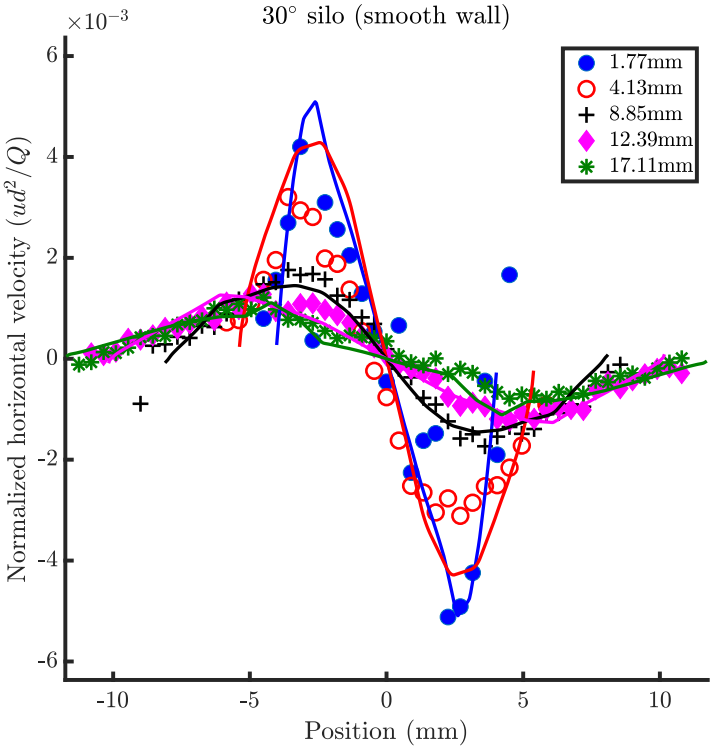

FIG. 7. The horizontal velocity MRI measurements (solid circles) compared with those predicted by the numerical model (lines) for the 30° silo at the same locations as in the vertical velocity figure.

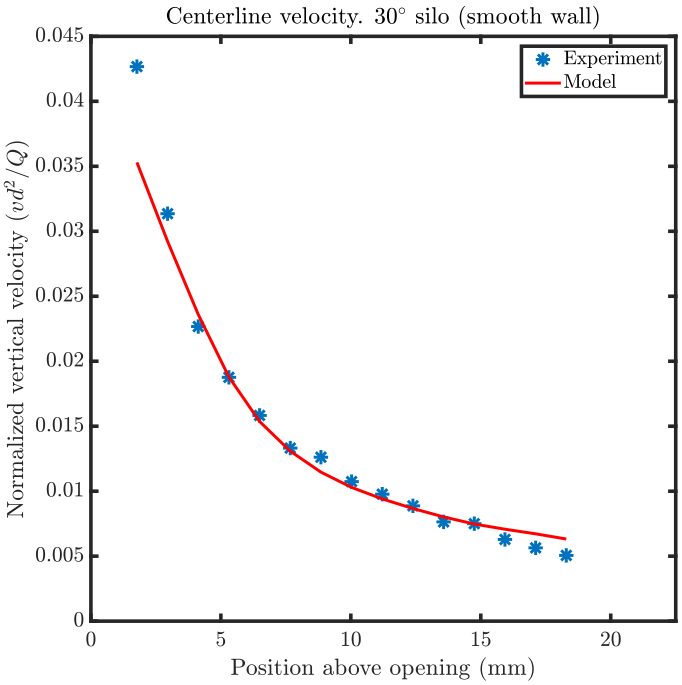

FIG. 8. A comparison of the normalized vertical velocity measured along the axial centerline of the silo compared with that predicted by the model for the 30° silo.

shape as the MRI experimental measurements. However, the absolute velocity predicted by the model does not match the experiment due to the discrepancy in the volumetric flow rate between the two. There is more noise in the horizontal measurements, and the prediction of normalized horizontal velocity is slightly worse near the silo opening, but overall the agreement is satisfying.

As a further test, in Fig. 8 we plot the normalized vertical component of velocity along the axial centerline of the silo and compare the experiment to the model. It is apparent that the model prediction is in very good agreement with the experimental results.

C. Numerical model results: 50° silo

In Sec. III B, the comparison of numerical and experimental velocity fields for the 30° silo with smooth walls, there were no stagnant regions in the flow domain. The transition from flowing to stationary is difficult to capture with simple incompressible Navier-Stokes–based models. Figures 9 and 10 show the normalized vertical and horizontal velocity measurements and predictions in the 50° silo. In this silo the distance from the silo opening to the transition point is ≈7.1 mm, and hence in this case two of our velocity contours are in the conical section, while the remaining three are in the cylindrical section.

Remarkably, the match between experimental and numerical model results is quite good. Despite the observed transition from a flowing to a stagnant state in the silo domain, the granular viscosity model is able to capture the (normalized) maximum velocity, the curvature and shape of the velocity contours, and the approximate location of the solid/flowing boundary.

Figure 11 compares the model to experimental normalized vertical velocity along the axial centerline of the 50° silo. In this case the experimentally measured velocity contains more noise than in the 30° case, but it is apparent that the model and experiment are similar and follow a somewhat similar decrease. However, the comparison is not quite as good as in the 30° case.

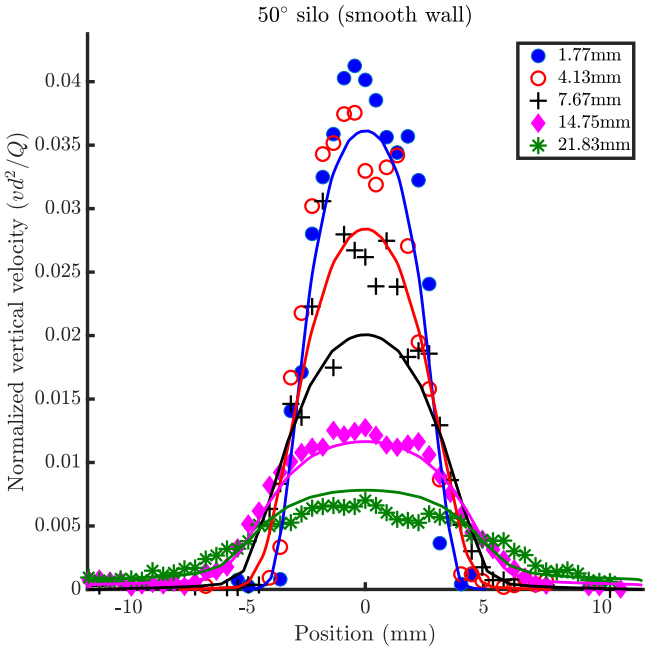

FIG. 9. The vertical velocity MRI measurements (solid circles) compared with those predicted by the numerical model (lines) for the 50° silo.

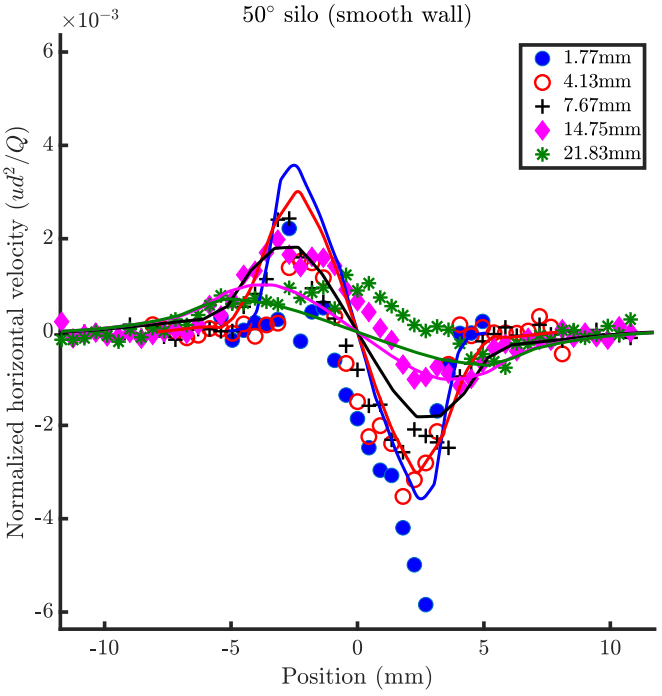

FIG. 10. The horizontal velocity MRI measurements (solid circles) compared with those predicted by the numerical model (lines) for the 50° silo at the same locations as in the vertical velocity figure.

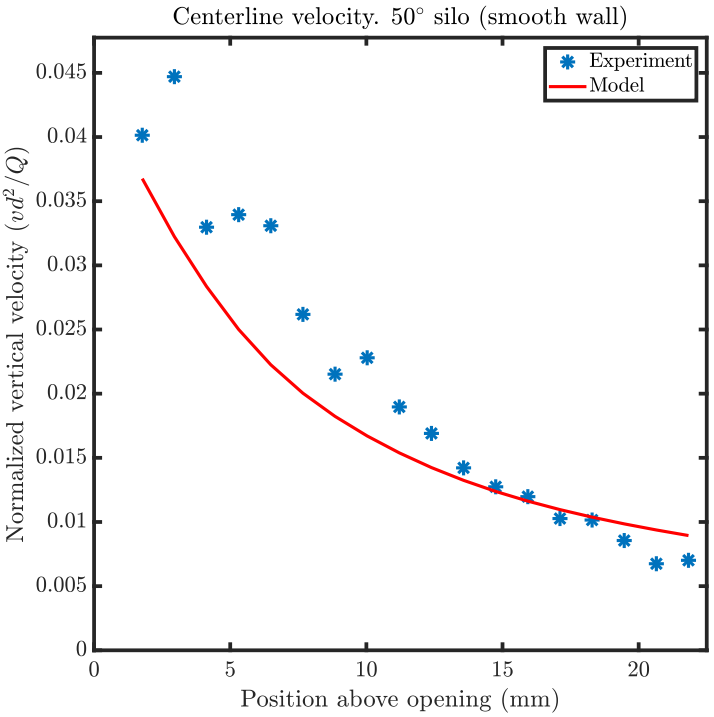

FIG. 11. A comparison of the normalized vertical velocity measured along the axial centerline of the silo compared with that predicted by the model for the 50° silo.

D. Numerical model results: 30° silo with rough walls

The most challenging flow regime to replicate is the rat-holing behavior observed in the 30° silo with roughened walls. In this case the observed magnitudes of horizontal velocity were too small to quantify since they were imperceptible from the experimental noise. Hence, the comparison of experimental to numerical predictions was only possible for the vertical velocity component. Figure 12 displays the normalized vertical velocity profile at five heights above the silo opening, while Fig. 13 is the normalized vertical velocity measured and predicted along the axial centerline of the silo.

It is apparent that the $\mu(I)$ model predictions completely fail to replicate the measured velocity, particularly far from the silo opening. In the case of rat-holing flow, the $\mu(I)$ model is unable to capture the observed dynamics.

E. Numerical model: Sensitivity analysis and flow rates

In order to further compare the experimental and numerical velocity predictions we compare predicted flow rates between the numerical and experimental results and perform a sensitivity analysis on the numerical model parameters.

To quantify the "goodness of fit" of the numerical predictions of velocity to the experimentally measured ones, we perform linear least-squares regression on the normalized vertical velocity data: $\widetilde{v}_{\text{num}} = b\widetilde{v}_{\text{exp}}$ (i.e., we force the regression to pass through the origin). In the case of a perfect fit between the numerical and experimental data, the slope of the line, b would be unity. The normalized vertical velocity data at five heights above the silo opening (the same heights as used in Figs. 6 and 9) are combined and the regression is performed on the entirety of this data at once. To test the sensitivity of the model predictions to model parameters this process was repeated 65 times for

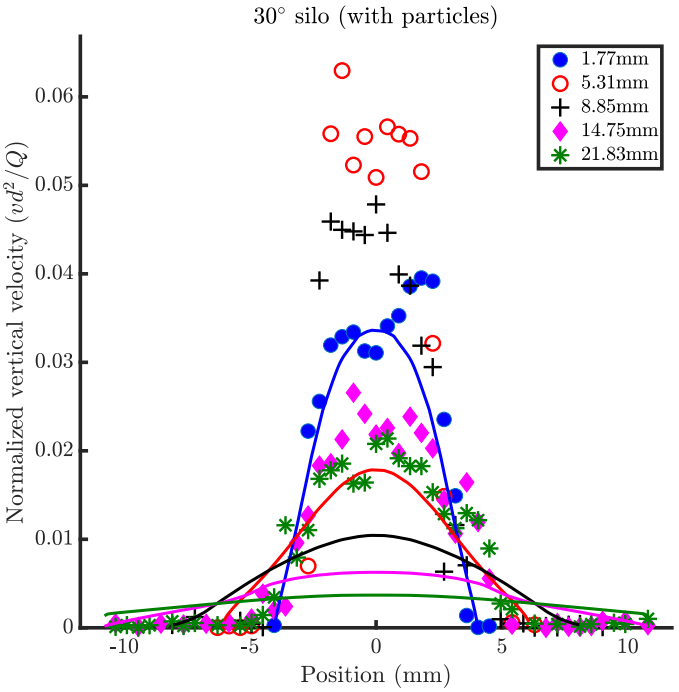

FIG. 12. The vertical velocity MRI measurements (solid circles) compared with those predicted by the numerical model (lines) for the 30° silo with roughened walls.

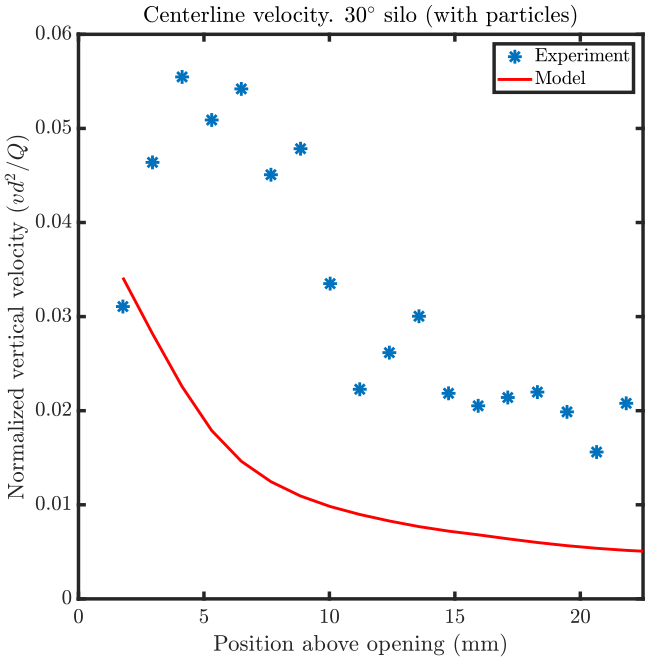

FIG. 13. A comparison of the normalized vertical velocity measured along the axial centerline of the silo compared with that predicted by the model for the 30° silo with roughened walls.

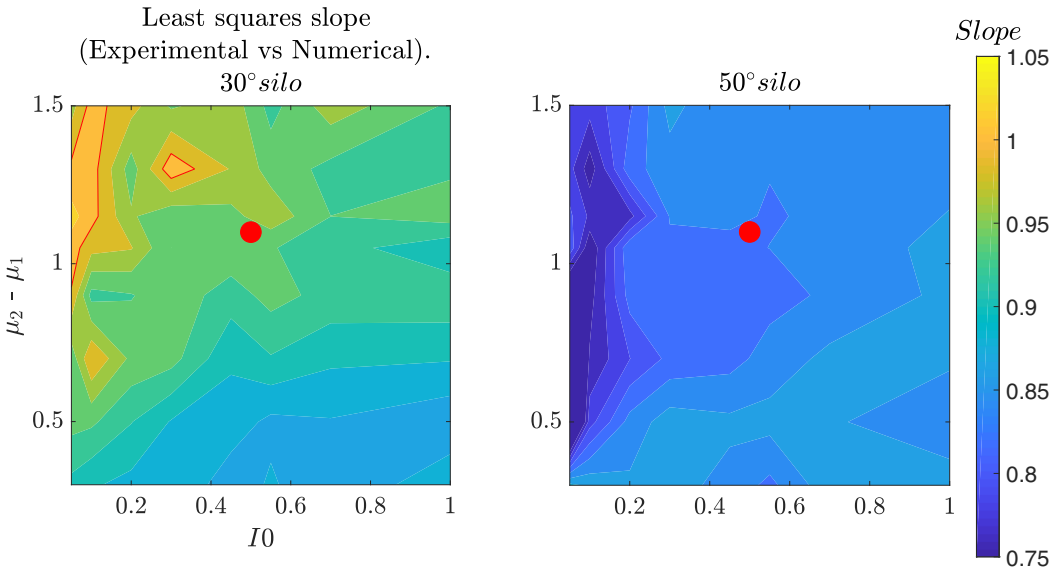

FIG. 14. Sensitivity analysis of the numerical model to parameters I_0 and μ_2-μ_1. The contour plots display the value of the slope found by performing a least-squares linear regression between the experimental and numerical normalized vertical velocity data. The left graph is the analysis for the 30° silo and the right for the 50° one. The red dot in the plots indicated the value of the parameters used in the current work, while the fine red line in the left plot is the contour of slope =1 (indicating a perfect fit of the numerical to experimental data).

different values of I_0 and μ_2. This analysis was performed for both the 30° and 50° silos, resulting in 130 numerical simulations. In each simulation the value of μ_1 was kept constant at 0.6, while the ranges of the other two parameters were $0.05 < I_0 < 1$ and $0.9 < \mu_2 < 2.1$. In Fig. 14 the slopes resulting from the linear least-squares regression analysis are contoured for the 30° (left) and 50° (right) silo flows, respectively. The solid red dot in the contour plots indicates the values of the parameters used in the current work to produce Figs. 6–13. The fine red line in the left plot is the contour of slope =1, which represents a perfect fit of the numerical prediction of normalized vertical velocity to its experimental measurement. In general, the 30° silo numerical simulation was better fit for lower I_0 and larger μ_2-μ_1 values, while the 50° simulation had the opposite behavior. The 30° simulation was always better fit to the experimental data than the 50° one, with reported slopes in the range 0.86 to 1.03 (by comparison, the 50° silo slopes were in the range 0.65 to 0.89). For the parameters used in the main text (see Table I) the least-squares slopes were 0.94 for the 30° silo and 0.84 for the 50° one. Overall, the choice of the parameters $I_0 = 0.5$ and $\mu_2 = 1.7$ used in this work is shown to be a good balance between accuracy for both the 30° and 50° silos.

Table II presents, for each of the three silos, the experimentally derived mass and volumetric flow rates, the numerically predicted volumetric flow rate, and an approximate solids volume fraction in

TABLE II. The experimentally derived and numerically predicted flow rates in the tested silos.

	$\dot{m}$ (g/s)	Q_{exp} (bulk, cm^3/s)	Q_{num} (cm^3/s)	$\sim\phi_{\text{exp}} = (\dot{m}/Q_{\text{exp}})/\rho_p$
30°	2.11 ± 0.07	4.54 ± 0.05	0.97	0.47 ± 0.02
50°	1.74 ± 0.09	3.8 ± 0.1	4.2	0.46 ± 0.04
30° (with particles)	2.2 ± 0.1	6.1 ± 0.3	0.81	0.36 ± 0.04

the bulk of the silo. The solids volume fraction in the bulk was approximated by taking the ratio of the experimental mass and volumetric flow rates (in the bulk of the silo) and then dividing by the particle density ($\approx$1000 kg/m^3). The predicted flowing solids fraction in the bulk of the 30° and 50° silos is remarkably similar (0.46 and 0.47, respectively). However, the 30° silo with particles glued to the wall shows a significantly lower solids volume fraction of 0.36. As previously noted, the numerical model was of incompressible type and hence was not able to accurately predict the correct flow rate. In the table the predicted volumetric flow rate in the 30° silo simulation was a factor of $\approx$4.5 smaller than the experimentally observed one. The volumetric flow rate predicted in the 50° silo simulation was a lot closer to the experimentally observed rate, but we caution against interpreting this as a validation of the model. During the sensitivity analysis the predicted flow rate varied by a factor of 10 over the ranges of the parameters tested, which indicates that it is sensitive to model parameter choice.

IV. DISCUSSION AND CONCLUSIONS

In this work we have presented results of experimental and numerical investigation of silo flow in three flow regimes: mass flow, funnel flow, and rat-holing. Using MRI velocimetry we measured both the horizontal and vertical components of velocity throughout the three test silos, including the transition from the converging conical to the cylindrical section. We found that the 30° silo produced a mass flow, the 50° silo produced a funnel flow, and the 30° silo with rough walls produced a rat-holing flow. We also presented results of a numerical model which used the $\mu(I)$ friction law to define an effective granular viscosity for dense granular flow. This viscosity was used to simulate the silo flows by means of incompressible computational fluid dynamics.

It was observed that the apparent volumetric flow rate in the MRI experiments was constant in the 30° silo but was a function of height above the silo opening for the other two; the flow rate was large near the silo opening but then rapidly fell to a near constant higher in the silo. The flow rate near the opening was roughly 2$\times$ that of the bulk, indicating that there is significant dilation of the flow near the silo exit opening in the 50° and 30° with rough wall cases. This is in contrast to the numerical model which enforced incompressibility of the flow. Recent studies have quantified the effect of solids fraction value at the silo opening on the flow rate from the silo [54] and reported that solids fraction in the near opening region could be as low as half that in the bulk of the silo. We conclude that to fully capture the experimental measurement of the flow rate (and, hence, the exact values of velocity) numerical models will likely need to include dilation effects, particularly for funnel and rat-holing flows. The effect of dilation for the mass-flow silo appeared negligible but may be important to accurately predict the volumetric flow rate from the silo.

To allow comparison between our experimental and numerical results, the velocity components of each were normalized by the local value of volumetric flow rate (i.e., the flow rate at height z above the silo opening). The resulting velocity fields derived from the 30° silo simulation showed excellent agreement with the experimental data. Plots of the vertical and horizontal velocity at a series of heights above the opening showed that both the shape and (normalized) maximum of the velocity contours were well matched, as was the vertical velocity component measured along the center line of the silo. The comparison in the 50° silo (which operated in the funnel-flow regime in the MRI experiment) were surprisingly impressive, with very good agreement between experimental and numerical results. This suggests that for appropriate values of fitting parameters the $\mu(I)$ friction law can be used to define an effective granular viscosity for granular dynamics, even in the case where there are transitions from static to flowing regions in the domain of study.

However, for the 30° silo with roughened walls (which displayed rat-holing in the MRI experiment), the simulation results were poorly matched to the experimental data. The grain dynamics in this silo are very complicated and hard to capture with numerical models. Rat-holing flow in a silo is often avoided by smoothing the silo walls (thus, changing the stress distribution in the silo) and/or increasing the size of the silo opening. It is a challenge for simple incompressible continuum viscoplastic models of granular flow to capture these "finite-particle-size" effects. Further work is

needed, including adding the effect of compressibility, to fully capture the observed dynamics in this situation.

It is clear that the $\mu(I)$ model performs admirably in a silo in the mass- and funnel-flow regimes for the parameter values chosen, but further model development is needed to fully capture the observed phenomena in rat-holing flow and to accurately predict the flow rate from the silo. Adding in a degree of compressibility into the model and/or accounting for granular nonlocality and finite-size effects may improve flow rate predictions in the silo and may help to capture more accurately flowing to stagnant phase transitions and potentially the rat-holing phenomenon [55]. Testing these hypotheses is currently being pursued by the authors. Additionally, the $\mu(I)$ friction law was discovered using experimental data from relatively low-friction spherical particles [56,57]. It is unclear whether the $\mu(I)$ model is the correct friction law to use for natural particles such as the poppy seeds used in this work. Furthermore, particle shape has been shown to be an important factor in the behavior of general granular systems [58,59] and silo systems specifically [60,61]. Using SEM imaging we found that our poppy seeds were kidney bean shaped and not spherical. Such an effect could be important to include in a numerical model of granular flow, although the factor does not seem critical, since we obtained very good agreement between experimental and numerical results for the 30° and 50° silos. The $\mu(I)$ parameters in the numerical model were our "best guess." The first friction coefficient, μ_1, was taken as the angle of repose of the poppy seeds; however, μ_2 and I_0 were chosen to be physically realistic and to try to reduce the ill-posed regions for the $\mu(I)$ model [50]. To check the dependence of model results on the I_0 and μ_2 parameters a sensitivity analysis was performed. It was found that the accuracy of the model was retained over a wide range of parameter values and that our choice of I_0 and μ_2 was a good balance of accuracy for both the 30° and 50° silos. To reduce model degrees of freedom these parameters should be measured for the specific set of particles [62]. In addition to experimentally quantifying model parameters, the development of realistic numerical boundary conditions should be a focus. Developing these boundary conditions is a significant future research challenge, but recent work has made excellent progress toward this goal [48,49]. The observation in the 30° silo that the flow regime changes from mass to rat-holing when the boundary condition is changed exemplifies the necessity of accurate boundary conditions and may indicate something more complex than a simple slip condition is needed. Finally, in recent times it has been shown that defining an effective granular viscosity using the $\mu(I)$ friction model with an incompressible flow assumption can be mathematically ill posed depending on the choice of parameters [63]. Adding the effect of compressibility seems to alleviate this issue [50,64]. Although we did not note any issues in our model for our choice of parameters, this fact serves as an additional motivation to transition to a compressible flow model of granular drainage from a silo.

ACKNOWLEDGMENTS

The authors acknowledge the Manawatu Microscopy Imaging Centre (MMIC) at Massey University for producing the SEM images of the poppy seeds in Fig. 1. L.F. also acknowledges funding from the Royal Society of New Zealand (Contracts No. RFT-15-MAU-001-PD and No. 17-MAU-029). Finally, we acknowledge the help of Maral Mehdizad and Alex Cliff to quantify the mass flow rates in the system.

[1] B. Andreotti, Y. Forterre, and O. Pouliquen, *Granular Media: Between Fluid and Solid* (Cambridge University Press, Cambridge, 2013).

[2] R. M. Nedderman, *Statics and Kinematics of Granular Materials* (Cambridge University Press, Cambridge, 2005).

[3] K. K. Rao and P. R. Nott, *An Introduction to Granular Flow* (Cambridge University Press, New York, 2008), Vol. 10.
[4] M. C. Garcia, H. J. Feise, S. Strege, and A. Kwade, Segregation in heaps and silos: Comparison between experiment, simulation and continuum model, Powder Technol. **293**, 26 (2016).
[5] T. Weinhart, C. Labra, S. Luding, and J. Y. Ooi, Influence of coarse-graining parameters on the analysis of dem simulations of silo flow, Powder Technol. **293**, 138 (2016).
[6] D. Bertuola, S. Volpato, P. Canu, and A. C. Santomaso, Prediction of segregation in funnel and mass flow discharge, Chem. Eng. Sci. **150**, 16 (2016).
[7] L. Staron, P.-Y. Lagrée, and S. Popinet, Continuum simulation of the discharge of the granular silo, Eur. Phys. J. E **37**, 5 (2014).
[8] L. Staron, P.-Y. Lagrée, and S. Popinet, The granular silo as a continuum plastic flow: The hour-glass vs the clepsydra, Phys. Fluids **24**, 103301 (2012).
[9] S. Volpato, R. Artoni, and A. C. Santomaso, Numerical study on the behavior of funnel flow silos with and without inserts through a continuum hydrodynamic approach, Chem. Eng. Res. Des. **92**, 256 (2014).
[10] Y. Wang and J. Y. Ooi, A study of granular flow in a conical hopper discharge using discrete and continuum approach, Procedia Eng. **102**, 765 (2015).
[11] S. Dunatunga and K. Kamrin, Continuum modeling and simulation of granular flows through their many phases, J. Fluid Mech. **779**, 483 (2015).
[12] L. A. Fullard, C. E. Davies, and G. C. Wake, Modelling powder mixing in mass flow discharge: A kinematic approach, Adv. Powder Technol. **24**, 499 (2013).
[13] L. Fullard, E. Breard, C. Davies, P.-Y. Lagrée, S. Popinet, and G. Lube, Testing the μ (i) granular rheology against experimental silo data, in *EPJ Web of Conferences* (EDP Sciences, Les Ulis, 2017), Vol. 140, p. 11002.
[14] Y. Zhou, P.-Y. Lagrée, S. Popinet, P. Ruyer, and P. Aussillous, Experiments on, and discrete and continuum simulations of, the discharge of granular media from silos with a lateral orifice, J. Fluid Mech. **829**, 459 (2017).
[15] L. A. Fullard, C. E. Davies, A. C. Neather, E. C. P. Breard, A. J. R. Godfrey, and G. Lube, Testing steady and transient velocity scalings in a silo, Adv. Powder Technol. **29**, 310 (2018).
[16] L. A. Fullard, C. E. Davies, G. Lube, A. C. Neather, E. C. P. Breard, and B. J. Shepherd, The transient dynamics of dilation waves in granular phase transitions during silo discharge, Granul. Matter **19**, 6 (2017).
[17] J. Choi, A. Kudrolli, and M. Z. Bazant, Velocity profile of granular flows inside silos and hoppers, J. Phys.: Condens. Matter **17**, S2533 (2005).
[18] A. Janda, I. Zuriguel, A. Garcimartín, L. A. Pugnaloni, and D. Maza, Jamming and critical outlet size in the discharge of a two-dimensional silo, Europhys. Lett. **84**, 44002 (2008).
[19] I. Sielamowicz, S. Blonski, and T. A. Kowalewski, Optical technique dpiv in measurements of granular material flows, part 1 of 3-plane hoppers, Chem. Eng. Sci. **60**, 589 (2005).
[20] K. Endo, K. A. Reddy, and H. Katsuragi, Obstacle-shape effect in a two-dimensional granular silo flow field, Phys. Rev. Fluids **2**, 094302 (2017).
[21] S. Waktola, A. Bieberle, F. Barthel, M. Bieberle, U. Hampel, K. Grudzień, and L. Babout, A new data-processing approach to study particle motion using ultrafast x-ray tomography scanner: Case study of gravitational mass flow, Exp. Fluids **59**, 69 (2018).
[22] K. Grudzien, M. Niedostatkiewicz, J. Adrien, E. Maire, and L. Babout, Analysis of the bulk solid flow during gravitational silo emptying using X-ray and ECT tomography, Powder Technol. **224**, 196 (2012).
[23] H.-Y. Xie and K. Shinohara, Measurement of solids velocity in a conical hopper by mass tracer particles, Chem. Eng. Sci. **54**, 455 (1999).
[24] P. A. Langston, M. S. Nikitidis, U. Tüzün, D. M. Heyes, and N. M. Spyrou, Microstructural simulation and imaging of granular flows in two-and three-dimensional hoppers, Powder Technol. **94**, 59 (1997).
[25] M. S. Nikitidis, U. Tüzün, and N. M. Spyrou, Determination of phase velocities in multi-phase flows in hoppers using dual photon gamma-ray tomography, Chem. Eng. Commun. **175**, 3 (1999).
[26] M. S. Nikitidis, U. Tüzün, and N. M. Spyrou, Tomographic measurements of granular flows in gases and in liquids, KONA Powder Part. J. **12**, 53 (1994).

[27] R. Stannarius, Magnetic resonance imaging of granular materials, Rev. Sci. Instrum. **88**, 051806 (2017).
[28] A. Penn, T. Tsuji, D. O. Brunner, C. M. Boyce, K. P. Pruessmann, and C. R. Müller, Real-time probing of granular dynamics with magnetic resonance, Sci. Adv. **3**, e1701879 (2017).
[29] C. M. Boyce, A. Penn, K. P. Prüssmann, and C. R. Müller, Magnetic resonance imaging of gas–solid fluidization with liquid bridging, AIChE J. **64**, 2958 (2018).
[30] C. M. Boyce, N. P. Rice, A. Ozel, J. F. Davidson, A. J. Sederman, L. F. Gladden, S. Sundaresan, J. S. Dennis, and D. J. Holland, Magnetic resonance characterization of coupled gas and particle dynamics in a bubbling fluidized bed, Phys. Rev. Fluids **1**, 074201 (2016).
[31] H. T. Fabich, A. J. Sederman, and D. J. Holland, Development of ultrafast ute imaging for granular systems, J. Magn. Reson. **273**, 113 (2016).
[32] C. M. Boyce, A. Ozel, N. P. Rice, G. J. Rubinstein, D. J. Holland, and S. Sundaresan, Effective particle diameters for simulating fluidization of non-spherical particles: CFD-DEM models vs. MRI measurements, AIChE J. **63**, 2555 (2017).
[33] H. T. Fabich, A. J. Sederman, and D. J. Holland, Study of bubble dynamics in gas-solid fluidized beds using ultrashort echo time (UTE) magnetic resonance imaging (MRI), Chem. Eng. Sci. **172**, 476 (2017).
[34] H. T. Fabich, T. I. Brox, D. Clarke, J. D. Seymour, S. L. Codd, P. Galvosas, J. Brown, A. J. Sederman, and D. J. Holland, Measurements of the velocity distribution for granular flow in a couette cell, Phys. Rev. E **98**, 062901 (2018).
[35] T. Kawaguchi, MRI measurement of granular flows and fluid-particle flows, Adv. Powder Technol. **21**, 235 (2010).
[36] M. Gentzler and G. I. Tardos, Measurement of velocity and density profiles in discharging conical hoppers by NMR imaging, Chem. Eng. Sci. **64**, 4463 (2009).
[37] Z. H. Gu, P. C. Arnold, and A. G. McLean, Prediction of the flowrate of bulk solids from mass flow bins with conical hoppers, Powder Technol. **72**, 157 (1992).
[38] P. Jop, Y. Forterre, and O. Pouliquen, A constitutive law for dense granular flows, Nature **441**, 727 (2006).
[39] P.-Y. Lagrée, L. Staron, and S. Popinet, The granular column collapse as a continuum: Validity of a two-dimensional Navier–Stokes model with a μ(I)-rheology, J. Fluid Mech. **686**, 378 (2011).
[40] P. B. Kowalczuk and J. Drzymala, Physical meaning of the sauter mean diameter of spherical particulate matter, Part. Sci. Technol. **34**, 645 (2016).
[41] K. To, Jamming transition in two-dimensional hoppers and silos, Phys. Rev. E **71**, 060301(R) (2005).
[42] N. Gui, X. Yang, J. Tu, and S. Jiang, Effects of rocking frequency and amplitude on particle discharge in rocking bed: A DEM study, Powder Technol. **292**, 31 (2016).
[43] A. McLean, The use of standpipes for increasing limiting gravitational flowrate from mass flow bins, KONA Powder Part. J. **11**, 139 (1993).
[44] C. Mankoc, A. Janda, R. Arevalo, J. M. Pastor, I. Zuriguel, A. Garcimartín, and D. Maza, The flow rate of granular materials through an orifice, Granul. Matter **9**, 407 (2007).
[45] W. A. Beverloo, H. A. Leniger, and J. Van de Velde, The flow of granular solids through orifices, Chem. Eng. Sci. **15**, 260 (1961).
[46] P. T. Callaghan, *Translational Dynamics and Magnetic Resonance*, 1st ed. (Oxford University Press, Oxford, 2011).
[47] S. Popinet, Gerris: A tree-based adaptive solver for the incompressible euler equations in complex geometries, J. Comput. Phys. **190**, 572 (2003).
[48] R. Artoni, A. C. Santomaso, M. Go, and P. Canu, Scaling Laws for the Slip Velocity in Dense Granular Flows, Phys. Rev. Lett. **108**, 238002 (2012).
[49] R. Artoni and A. Santomaso, Effective wall slip in chutes and channels: Experiments and discrete element simulations, Granul. Matter **16**, 377 (2014).
[50] T. Barker, D. G. Schaeffer, M. Shearer, and J. M. N. T. Gray, Well-posed continuum equations for granular flow with compressibility and μ(I)-rheology, Proc. R. Soc. A **473**, 20160846 (2017).
[51] L. Fullard and C. Davies, Minimising the spread of residence-time distribution for flat and heaped powders in a wedge-shaped planar hopper, Particuology **30**, 102 (2017).
[52] K. E. Fickie, R. Mehrabi, and R. Jackson, Density variations in a granular material flowing from a wedge-shaped hopper, AIChE J. **35**, 853 (1989).

[53] R. L. Brown, Minimum energy theorem for flow of dry granules through apertures, Nature **191**, 458 (1961).
[54] M. Benyamine, P. Aussillous, and B. Dalloz-Dubrujeaud, Discharge flow of a granular media from a silo: Effect of the packing fraction and of the hopper angle, in *EPJ Web of Conferences* (EDP Sciences, Les Ulis, 2017), Vol. 140, p. 03043.
[55] D. L. Henann and K. Kamrin, A predictive, size-dependent continuum model for dense granular flows, Proc. Natl. Acad. Sci. USA **110**, 6730 (2013).
[56] G. D. R. MiDi, On dense granular flows, Eur. Phys. J. E **14**, 341 (2004).
[57] P. Jop, Y. Forterre, and O. Pouliquen, Crucial role of sidewalls in granular surface flows: Consequences for the rheology, J. Fluid Mech. **541**, 167 (2005).
[58] E. Azéma, N. Estrada, I. Preechawuttipong, J.-Y. Delenne, and F. Radjai, Systematic description of the effect of particle shape on the strength properties of granular media, in *EPJ Web of Conferences* (EDP Sciences, Les Ulis, 2017), Vol. 140, p. 06026.
[59] S. Zhao and X. Zhou, Effects of particle asphericity on the macro-and micro-mechanical behaviors of granular assemblies, Granul. Matter **19**, 38 (2017).
[60] T. Börzsönyi, E. Somfai, B. Szabó, S. Wegner, A. Ashour, and R. Stannarius, Elongated grains in a hopper, in *EPJ Web of Conferences* (EDP Sciences, Les Ulis, 2017), Vol. 140, p. 06017.
[61] E. Goldberg, C. M. Carlevaro, and L. A. Pugnaloni, Effect of grain shape on the jamming of two-dimensional silos, in *EPJ Web of Conferences* (EDP Sciences, Les Ulis, 2017), Vol. 140, p. 06009.
[62] A. Fall, G. Ovarlez, D. Hautemayou, C. Mézière, J.-N. Roux, and F. Chevoir, Dry granular flows: Rheological measurements of the μ(I)-rheology, J. Rheol. **59**, 1065 (2015).
[63] T. Barker, D. G. Schaeffer, P. Bohorquez, and J. M. N. T. Gray, Well-posed and ill-posed behavior of the $\mu(I)$-rheology for granular flow, J. Fluid Mech. **779**, 794 (2015).
[64] J. Heyman, R. Delannay, H. Tabuteau, and A. Valance, Compressibility regularizes the μ(I)-rheology for dense granular flows, J. Fluid Mech. **830**, 553 (2017).